Magnetic Resonance Imaging 102 (2023) 103–114

Contents lists available at ScienceDirect

Magnetic Resonance Imaging

journal homepage: www.elsevier.com/locate/mri

Evaluation of simultaneous multi-slice readout-segmented diffusion-weighted MRI acquisition in human optic nerve measurements

Hiromasa Takemura [a,b,c,*], Wei Liu [d], Hideto Kuribayashi [e], Toshikazu Miyata [a,b,f], Ikuhiro Kida [a,f]

[a] Center for Information and Neural Networks (CiNet), Advanced ICT Research Institute, National Institute of Information and Communications Technology, Suita, Japan
[b] Division of Sensory and Cognitive Brain Mapping, Department of System Neuroscience, National Institute for Physiological Sciences, Okazaki, Japan
[c] Graduate Institute for Advanced Studies, SOKENDAI, Hayama, Japan
[d] Siemens Shenzhen Magnetic Resonance Ltd., Shenzhen, China
[e] Siemens Healthcare K.K., Tokyo, Japan
[f] Graduate School of Frontier Biosciences, Osaka University, Suita, Japan

ARTICLE INFO

Keywords:
diffusion MRI
tractography
readout-segmented EPI
visual system

ABSTRACT

Diffusion-weighted magnetic resonance imaging (dMRI) is the only available method to measure the tissue properties of white matter tracts in living human brains and has opened avenues for neuroscientific and clinical studies on human white matter. However, dMRI using conventional simultaneous multi-slice (SMS) single-shot echo planar imaging (ssEPI) still presents challenges in the analyses of some specific white matter tracts, such as the optic nerve, which are heavily affected by susceptibility-induced artifacts. In this study, we evaluated dMRI data acquired by using SMS readout-segmented EPI (rsEPI), which aims to reduce susceptibility-induced artifacts by dividing the acquisition space into multiple segments along the readout direction to reduce echo spacing. To this end, we acquired dMRI data from 11 healthy volunteers by using SMS ssEPI and SMS rsEPI, and then compared the dMRI data of the human optic nerve between the SMS ssEPI and SMS rsEPI datasets by visual inspection of the datasets and statistical comparisons of fractional anisotropy (FA) values. In comparison with the SMS ssEPI data, the SMS rsEPI data showed smaller susceptibility-induced distortion and exhibited a significantly higher FA along the optic nerve. In summary, this study demonstrates that despite its prolonged acquisition time, SMS rsEPI is a promising approach for measuring the tissue properties of the optic nerve in living humans and will be useful for future neuroscientific and clinical investigations of this pathway.

1. Introduction

Advancements in diffusion-weighted magnetic resonance imaging (dMRI) and tractography algorithms have enabled identification of major white matter tracts in living human brains [1–7]. This method has opened up avenues to evaluate the tissue properties of white matter tracts in individuals and compare them with distributions in a healthy population [8]. This approach has been confirmed to be useful for understanding the effects of retinal disorders on white matter [9–12], the relationship between language-related white matter tracts and reading performance [13–16], the relationship between white matter tracts in the limbic system and psychiatric disorders [17], age dependency of white matter tissue properties [18–20], and lateralization of white matter tracts [21–23].

Although dMRI studies can provide insights into the field of cognitive and clinical neuroimaging, the existing methods show several limitations. Researchers usually acquire dMRI data using single-shot echo planar imaging (ssEPI). However, dMRI data acquired using ssEPI often shows image distortions and signal dropout due to susceptibility-induced artifacts in the brain areas near the paranasal sinus or petrous apex/mastoid air complexes. This limitation poses challenges in identifying white matter pathways in areas affected by susceptibility-induced artifacts, such as the optic nerve, which is located near the paranasal sinus. Assessment of the optic nerve is essential to evaluate the impact of disease by which it is directly damaged, such as optic neuritis [24] and glaucoma [12,25,26]. In addition, dMRI measurements of the

* Corresponding author at: Division of Sensory and Cognitive Brain Mapping, Department of System Neuroscience, National Institute for Physiological Sciences, 38 Nishigonaka Myodaiji, Okazaki, Aichi 444-8585, Japan.
E-mail address: htakemur@nips.ac.jp (H. Takemura).

https://doi.org/10.1016/j.mri.2023.05.001
Received 31 March 2022; Received in revised form 2 May 2023; Accepted 2 May 2023
Available online 4 May 2023

optic nerve is important in understanding how amblyopia [27,28] affects white matter pathways; amblyopia commonly affects only one eye and its optic nerve has to be compared to that of the other eye. While obtaining dMRI measurements of the optic nerve using the conventional ssEPI method is not impossible [26,29,30], challenges in measurements limit the opportunity to study the optic nerve in relation to the health and diseases of the human visual system [31].

A few approaches have been proposed to improve dMRI measurements of the optic nerve. One approach is EPI acquisition with a reduced field of view to achieve higher image quality [32–36]. However, this approach limits the opportunity to evaluate the optic nerve along with other visual pathways, such as the optic tract and optic radiation, using the same dataset. An alternative approach is to use multi-shot EPI readout for dMRI acquisition to reduce echo spacing and achieve a higher resolution while reducing artifacts. The use of a multi-shot EPI approach for dMRI measurement of the human optic nerve has already been proposed [37], and various multi-shot methods for dMRI data acquisitions have been proposed to reduce the limitations of dMRI measurements using ssEPI [38–45]. Readout-segmented echo-planar imaging (rsEPI) is a multi-shot method that divides the acquisition space (k-space) into multiple segments along the readout direction (multi-shot acquisition) to enable the acquisition of dMRI data with a shorter echo time, reduced echo spacing, and reduced echo train length [46]. Several clinical studies have demonstrated that rsEPI is a useful approach for evaluation of the optic nerve and optic chiasm as it provides superior image quality with less distortion than ssEPI [47–52]. In addition, using rsEPI, a recent study identified the olfactory tract, a white matter tract affected by susceptibility-induced artifacts, from the dMRI data acquired from living humans [93]. However, a major limitation of multi-shot EPI methods, including rsEPI, is the prolonged acquisition time because of the need to collect data from multiple segments [53]. The prolonged acquisition time of rsEPI limits its application when whole-brain acquisition and tractography are required, as such studies require data acquisition from a large number of slices and diffusion gradient directions.

Frost et al. (2015) proposed combining simultaneous multi-slice (SMS) acquisition [54–56] and rsEPI to overcome the prolonged acquisition time in rsEPI [57]. This method, named SMS rsEPI, could substantially reduce the dMRI acquisition time in comparison with rsEPI acquisition without SMS [57]. Thus, the development of SMS rsEPI methods has made dMRI measurements with rsEPI more practical for neuroscience and clinical studies. However, the brain areas in which dMRI acquisition with SMS rsEPI has an advantage over the commonly used SMS ssEPI method remain unclear.

This study aimed to evaluate the advantage of SMS rsEPI over SMS ssEPI in a tract-specific analysis of dMRI datasets on living human brains. To this end, we acquired dMRI data from 11 healthy volunteers by using both SMS rsEPI and SMS ssEPI. SMS ssEPI data were acquired multiple times to match the scan time with SMS rsEPI. We performed experiments with two different voxel sizes to evaluate the generality of findings. In our data analysis, we primarily focused on the optic nerve, which is commonly affected by susceptibility-induced artifacts, to clarify whether SMS rsEPI is an advantageous method for the measurement of this tract.

2. Material and methods

2.1. Participants

Eleven healthy participants (mean age: 23.8 years; age range: 19–34 years; four females) participated in this study. All participants had normal or corrected-to-normal vision and participated in two experiments (Experiment 1 and Experiment 2). The study protocol was approved by the local ethics and safety committees at Center for Information and Neural Networks (CiNet), Advanced ICT Research Institute, National Institute of Information and Communications Technology (NICT) and conducted in accordance with the ethical standards stated in the Declaration of Helsinki. Written informed consent was obtained from all participants.

2.2. MRI acquisition method

All MRI data were acquired using the SIEMENS 3 T scanner (MAGNETOM Prisma, Siemens Healthcare, Erlangen, Germany) at CiNet, NICT, with the 32-channel head coil. The T1-weighted MRI data and all dMRI data were acquired during the same session.

2.2.1. T1-weighted MRI data acquisition

We obtained T1-weighted magnetization-prepared rapid gradient-echo (MP-RAGE) images (voxel size: 1 mm isotropic; repetition time [TR]: 1990 ms; echo time [TE]: 3.37 ms; inversion time: 900 ms) from all participants. This image was used to identify regions of interest (ROIs) for tractography analysis and to estimate the border between the white and gray matter in subsequent analyses (see below). This image was also used as a reference image when evaluating distortions of dMRI images (see Fig. 2).

2.2.2. dMRI data acquisition

2.2.2.1. Experiment 1. Experiment 1 aimed to evaluate dMRI data acquired with a relatively coarse voxel size that is often used for DTI analysis. To this end, we acquired dMRI data using spin-echo echo planar imaging (EPI) with 2 mm isotropic voxels and 30 isotropically distributed diffusion weighting at $b = 1000$ s/mm^2 (field of view [FoV]: 200 × 200 × 144 mm^3; number of slices: 72; diffusion scheme: monopolar). We acquired two dMRI image sets: one was acquired using the SMS ssEPI sequence (TR: 4000 ms; TE: 65 ms; echo spacing [ES]: 0.65 ms; echo train length: 32.5 ms) and the other was acquired using the SMS rsEPI sequence, which is a work-in-progress sequence (research sequence) provided by SIEMENS (number of readout segments: 5; TR: 4390 ms; TE: 54 ms; ES: 0.34 ms; echo train length: 17 ms). Of note, the TR used for SMS ssEPI was the same in both experiments and above the minimum value. SMS rsEPI data was acquired with the reacquisition scheme, which was proposed in previous studies [46,57]. Both dMRI image sets were acquired with SMS excitation (SMS factor: 2) using blipped Controlled Aliasing In Parallel Imaging Results In Higher Acceleration (CAIPIRINHA) [58], in-plane acceleration (iPAT: 2) using generalized autocalibrating partially parallel acquisitions (GRAPPA) [59], and posterior-anterior phase-encoding direction with no slice gap. The slice orientation was transverse. Phase partial Fourier was not applied for the acquisition of either image set. Four non-diffusion-weighted ($b = 0$) images (hereafter called "low b-value images") were acquired for each image set. During the acquisition of each image set, one low b-value image was acquired at the beginning and three at the end. In addition, we acquired two low b-value images with a reversed phase-encoding direction (anterior-posterior) for each image set. dMRI acquisition with SMS ssEPI was repeated five times to match the scan time with SMS rsEPI (SMS rsEPI: 13 min 11 s; SMS ssEPI: 12 min 55 s for five repetitions). For six participants, we acquired the SMS ssEPI image set earlier than the SMS rsEPI image set. For the remaining five participants, we acquired the SMS rsEPI image set earlier than the SMS ssEPI image set. The details of the acquisition parameters are listed in Table 1.

2.2.2.2. Experiment 2. Experiment 2 aimed to evaluate the dMRI dataset acquired with relatively smaller voxel size. To this end, we acquired dMRI data by using spin-echo EPI with 1.8-mm isotropic voxels and 30 isotropically distributed diffusion weighting at $b = 1000$ s/mm^2 (FoV: 198 × 198 × 129.6 mm^3; number of slices: 72; diffusion scheme: monopolar). The data acquisition methods were largely the same as those used in Experiment 1, except for the following points. First, acquisition parameters differed slightly from those in Experiment 1 in

Table 1
Acquisition parameters for dMRI experiment. ES: Echo Spacing, Diff. dir.: Diffusion directions, rep.: repetitions.

	Voxel Size (mm)	# Readout Segments	ES (ms)	SMS factor	iPAT	TR (ms)	TE (ms)	b (s/mm^2)	#b = 0/ Diff. dir.	Scan time (min)
Experiment 1 ($N = 11$)										
SMS rsEPI	2 iso	5	0.34	2	2	4390	54	1000	4/30	13:11
SMS ssEPI	2 iso	–	0.65	2	2	4000	65	1000	4/30	12:55 (5 rep.)
Experiment 2 ($N = 11$)										
SMS rsEPI	1.8 iso	5	0.34	2	2	4520	56	1000	4/30	13:34
SMS ssEPI	1.8 iso	–	0.70	2	2	4000	70	1000	4/30	13:05 (5 rep.)

both SMS ssEPI (TR: 4000 ms; TE: 70 ms; ES: 0.70 ms; echo train length: 38.5 ms) and SMS rsEPI (TR: 4520 ms; TE: 56 ms; ES: 0.34 ms; echo train length: 18.7 ms). Second, the acquisition time differed from that in Experiment 1 (SMS rsEPI: 13 min 34 s; SMS ssEPI: 13 min 5 s for five repetitions). The details of the acquisition parameters are listed in Table 1.

Both imaging and diffusion gradients were taken into account in the b-matrix calculations, which were used for subsequent analyses, in the SMS ssEPI and SMS rsEPI sequences.

2.2.2.3. Behavioral task. During dMRI data acquisition, we instructed the participants to perform a fixation task to minimize eye movements. The participants viewed an MR-compatible screen monitor (BOLDscreen 32, Cambridge Research Systems, Kent, UK) located at the exit of the magnet bore via a mirror mounted over their eyes. A fixation point was presented at the center of the screen with a gray background. The participants were instructed to press a button when the color of the fixation dot (green or red) changed. The change in the fixation color occurred at a random timing once per 4 s on average. The participants were able to respond to changes in the fixation color within 1 s on most occasions (mean and standard deviation: 92.66% ± 10.19% for all participants), suggesting that eye movements are minimized during dMRI data acquisition.

2.3. MRI analysis method

2.3.1. T1-weighted MRI data processing

T1-weighted images were aligned to the AC-PC (anterior commissure-posterior commissure) space by using vistasoft (https://github.com/vistalab/vistasoft). We then performed tissue segmentation on T1-weighted images by using an automated procedure implemented in FreeSurfer (recon-all; [60]) and FSL (FAST; [61]). These segmentations were used to define the ROIs and perform tractography in subsequent analyses (see below).

2.3.2. dMRI data preprocessing

We performed susceptibility-induced distortion correction in the dMRI data by using the FSL TOPUP tool [62]. While we performed image comparisons of dMRI data before and after this correction (see Results), all subsequent analyses were performed based on the dMRI data with susceptibility-induced distortion correction. The dMRI data were corrected for eddy-current distortions and participant motion by using the FSL EDDY tool [63], and then aligned with T1-weighted MRI data by using a 14-parameter constrained nonlinear registration in the vistasoft distribution (mrDiffusion; https://github.com/vistalab/vistasoft). B-matrices were reoriented after eddy-current correction and co-registration with T1-weighted images by applying the same transformation for the dMRI images [64]. We fit the diffusion tensor model to the dMRI data by using RESTORE (Robust Estimation of Tensors by Outlier Rejection; [65]). The resulting eigenvalues in each voxel were used to compute the FA, axial diffusivity (AD), and radial diffusivity (RD) [66] according to following formula:

$$FA = \sqrt{\frac{1}{2}} * \frac{\sqrt{(\lambda_1 - \lambda_2)^2 + (\lambda_2 - \lambda_3)^2 + (\lambda_3 - \lambda_1)^2}}{\sqrt{\lambda_1{}^2 + \lambda_2{}^2 + \lambda_3{}^2}} \quad (1)$$

$$AD = \lambda_1 \quad (2)$$

$$RD = (\lambda_2 + \lambda_3)/2 \quad (3)$$

where λ_1, λ_2, and λ_3 are three eigenvalues obtained by fitting the diffusion tensor model. Among these eigenvalues, λ_1 is the principal eigenvalue of the diffusion tensor model.

In addition, we also fitted constrained spherical deconvolution (CSD) for subsequent tractography analysis of major white matter tracts by using MRTrix3 (https://www.mrtrix.org/; [67]). For the dMRI data acquired with SMS ssEPI, fitting of tensor model and CSD was performed for the data combined across multiple repetitions.

2.3.3. Defining ROIs for tractography on visual pathways

We defined ROIs for tractography on the T1-weighted images acquired from each subject, which were defined using the methods already established in previous studies [8–11,26].

2.3.3.1. Optic nerve head. We manually defined the position of the optic nerve head by visual inspection of a T1-weighted image in accordance with the method used in a previous study [26]. The ROIs for the optic nerve head were a 4-mm radius sphere centered slightly posterior to the optic nerve head at the back of the eye (Supplementary Fig. 1).

2.3.3.2. Optic chiasm. The optic chiasm ROI was identified from the T1-weighted image using an automated segmentation pipeline implemented in FreeSurfer (recon-all; [60]).

2.3.3.3. Lateral geniculate nucleus. The lateral geniculate nucleus (LGN) was identified using methods described in previous publications [9–11]. In brief, we performed deterministic tractography by defining the optic chiasm as a seed to determine streamline termination near the LGN. We then defined the LGN ROIs as a 4-mm radius sphere that covered the endpoints of the streamlines from the optic chiasm. The anatomical validity of this method was evaluated in a previous study based on a comparison with histological data [11].

2.3.3.4. Primary visual cortex. The ROI for the primary visual cortex (V1) was identified from the T1-weighted image using the Brodmann atlas implemented in the FreeSurfer pipeline [60,68].

2.3.4. Tractography

We performed tractography on the dMRI data to identify the white matter tracts in each participant. We used tractography algorithms, tractography parameters, and streamline exclusion criteria, that have already been established in previous studies to identify each white matter tract [8–11,26].

2.3.4.1. Optic nerve. We identified the optic nerve using a method described in a previous study [26]. Specifically, we used CSD-based probabilistic tractography (iFOD2) implemented in MRTrix3 (fiber orientation distribution amplitude cutoff: 0.01; minimum streamline length: 20; maximum streamline length: 100) [69] and generated 5000 streamlines between a pair of ROIs (left/right optic nerve head and optic chiasm). We used this method because it is difficult to identify the optic nerve using tensor-based probabilistic tractography or whole-brain tractography owing to the relatively lower signal quality in this area. After generating streamlines between ROIs, we removed streamlines that met the following criteria: (1) streamline length $\geq$ 3 S.D. longer than the median streamline length in the tract and (2) streamline position $\geq$3 S.D. away from the median position of the tract [8]. This removal step was repeated three times. Finally, we rejected streamlines whose median distance to the tract core among all nodes was larger than 4.5 mm. Fig. 1 and Supplementary Fig. 2 show the optic nerve identified by tractography.

2.3.4.2. Optic tract. We identified the optic tract using ConTrack [70] with the methods described in previous studies [9,11]. We sampled 5000 candidate streamlines connecting the optic chiasm and LGN (angle threshold: 90°; step size: 1 mm; maximum streamline length: 80 mm) in both hemispheres. We then selected the 100 streamlines with the highest scores in the ConTrack scoring process [71].

2.3.4.3. Optic radiation. We identified the optic radiation using ConTrack [70], which is known to have sufficient sensitivity to identify the optic radiation, including Meyer's loop, from relatively low-resolution DTI data [71]. Using ConTrack, we sampled 100,000 candidate streamlines connecting the LGN and V1 (angle threshold: 90°; step size: 1 mm; maximum streamline length: 240 mm). We sampled a larger number of candidate streamlines for the optic radiation in comparison with those used for the optic nerve and optic tract, since the optic radiation has a larger volume and crosses other fibers in the Meyer's loop region [72]. Tracking was restricted using a white matter mask generated by tissue segmentation by FSL FAST.

We refined the optic radiation streamlines on the basis of an outlier rejection process. First, we selected 30,000 streamlines with the highest scores in the ConTrack scoring process [71]. Next, we removed streamlines passing through voxels where the mean diffusivity exceeded 1 μm^2/ms to minimize partial voluming with lateral ventricles. Third, using manually defined "NOT" ROIs, we excluded streamlines passing through the corpus callosum, anterior commissure, or brainstem or traversing the white matter inferior to the hippocampus as biologically implausible streamlines. Finally, we further removed streamlines based on the following criteria: (1) streamline length $\geq$ 3 S.D. longer than the median streamline length in the tract and (2) streamline position $\geq$3 S.D. away from the median position of the tract [8]. ConTrack has been used to successfully identify the optic radiation in previous publications [9–12,71,73–79].

2.3.4.4. Other major white matter tracts. We also identified other major white matter tracts to evaluate the extent to which the effect observed in the visual pathways can be generalized to other parts of the white matter. To this end, we generated whole-brain streamlines by using CSD-based probabilistic tractography implemented in MRTrix3 (iFOD2) [67] and taking the gray matter/white matter interface region, which was defined based on FSL FAST, as the seed voxels [80]. Two million streamlines were generated using the default parameters (step size: 0.5 x voxel size; angle, 45 deg.; minimum length of streamline: 2 x voxel size; maximum length of streamline: 100 x voxel size; fiber orientation distribution amplitude cutoff, 0.1). We identified the corticospinal tract (CST), forceps major, forceps minor, and inferior longitudinal fasciculus (ILF) from whole-brain streamlines by using the AFQ MATLAB toolbox (https://github.com/yeatmanlab/AFQ) [8]. After identifying each tract, outlier streamlines were further excluded using the following criteria: (1) streamline length > 4 S.D. longer than the median streamline length in the tract and (2) streamline position >4 S.D. away from the median position of the tract.

2.4. Evaluation of tissue properties along the tract

We evaluated the tissue properties of each visual white matter tract using methods used in previous studies [8,9,11,73,75,79]. Briefly, each streamline was resampled to 100 equidistant nodes. The tissue properties (FA, AD, and RD) were calculated for each node in each streamline. The properties at each node were summarized by taking the weighted average of the tissue properties (such as FA values) on each streamline within that node. The weight of each streamline was based on the Mahalanobis distance from the tract core. We excluded the first and last 10 nodes from the tissue property of the tract core to exclude voxels close to gray/white matter interfaces, where the tract was likely to intersect heavily with other tracts. We summarized the profile of each tract with a vector of 80 values representing FA, AD, and RD sampled at equidistant locations along the central portion of the tract. We calculated the average FA, AD, and RD values among 80 nodes for comparisons between the SMS rsEPI and SMS ssEPI datasets in each tract.

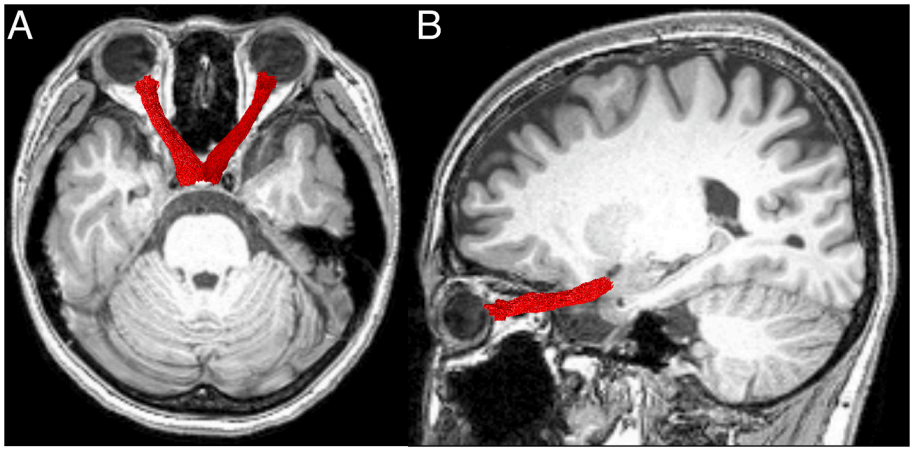

Fig. 1. The optic nerve identified in a representative participant (participant P1). The optic nerve (red) overlaid on a slice of a T1-weighted image (A. axial; B. sagittal, left hemisphere). The optic nerve was identified on SMS rsEPI data acquired in Experiment 1. (For interpretation of the references to colour in this figure legend, the reader is referred to the web version of this article.)

2.5. Statistical comparisons

For each tract, we performed a two-tailed two-sample *t*-test on FA to evaluate the statistical differences between the SMS rsEPI and SMS ssEPI datasets. We defined statistical significance (α) as $P = 0.004$, which is equivalent to Bonferroni correction for 12 comparisons (left/right optic nerve, left/right optic tract, left/right optic radiation, left/right CST, forceps major, forceps minor, and left/right ILF). We also calculated Cohen's d to estimate the effect size of the difference in FA between the SMS rsEPI and SMS ssEPI datasets. Statistical analyses were performed by using the MATLAB Statistics and Machine Learning Toolbox.

In addition, we performed a supplementary analysis to compare FA along the optic nerve between images acquired with different voxel sizes (Experiment 1 and 2) by performing a two-tailed two-sample *t*-test. We defined α as $P = 0.05$ in this supplementary analysis.

3. Results

3.1. Qualitative comparisons of image quality

Figure 2 compares the T1-weighted image (panel A) with low b-value and diffusion-weighted images acquired with SMS rsEPI and SMS ssEPI (panel B). These images were axial images including the optic nerve. The left two columns of Fig. 2B show the images before applying susceptibility-induced distortion corrections. SMS ssEPI data showed susceptibility-induced image distortions near the optic nerve, which was located close to the paranasal sinus (the location of eyeballs in a T1-weighted image is overlaid as yellow dotted lines in Fig. 2B). In contrast, SMS rsEPI data evidently showed smaller amounts of distortions at the optic nerve than the SMS ssEPI data in both Experiment 1 and 2 datasets (Fig. 2B). In addition to reduction of image distortions near the optic nerve, SMS rsEPI data also showed smaller amounts of image distortions and signal pile-up at the posterior part of the temporal lobe in these axial slices, which is near the petrous apex and mastoid air complexes (the location of the posterior end of the temporal pole in this slice is also shown as yellow dotted lines in Fig. 2B). Both SMS rsEPI and SMS ssEPI data did not show significant image distortions in the cerebellum (Fig. 2B).

The two right columns of Fig. 2 depict images after susceptibility-induced distortion correction using the FSL TOPUP tool [62]. After correction, image distortions near the optic nerve in SMS ssEPI data were substantially reduced, and assessment of image quality differences solely by visual inspection was difficult (see Supplementary Fig. 3 for images acquired from other participants). In the subsequent analysis of diffusivity and its statistical comparisons, we focused on the data after the susceptibility-induced distortion.

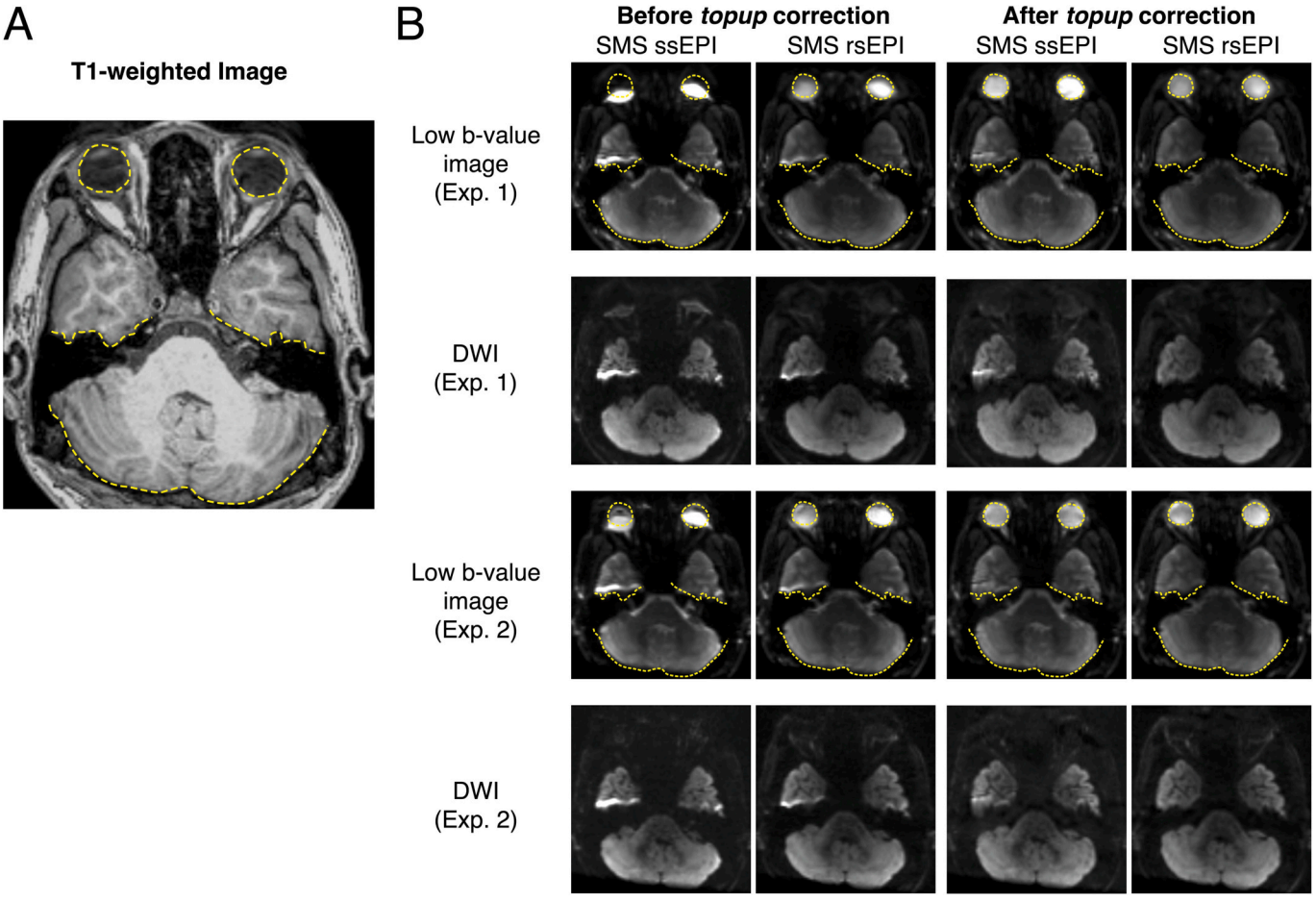

Fig. 2. Comparison of image quality of SMS rsEPI and SMS ssEPI data for the optic nerve. A. An axial section of a T1-weighted image of a representative participant (participant P3), which includes the optic nerve. Yellow dotted lines depict the contours of eyeballs, the posterior border of the temporal pole, and the cerebellum as a reference to understand image distortions in dMRI data. B. Axial image of the dMRI dataset acquired from participant P3. The position of the axial section corresponds to that in panel A. Each panel depicts an axial image of low b-value or diffusion-weighted images (DWI), which includes the optic nerve (left two columns, images before FSL TOPUP distortion correction; right two columns, images after distortion correction). The top two rows depict images acquired in Experiment 1, whereas the bottom two rows depict images acquired in Experiment 2. Yellow dotted lines as shown in panel A are overlaid on low b-value images. (For interpretation of the references to colour in this figure legend, the reader is referred to the web version of this article.)

3.2. Statistical comparison of diffusivity measurements in visual pathways

3.2.1. Optic nerve

Using tractography, we successfully identified the optic nerve in both hemispheres in all participants (Fig. 1 and Supplementary Fig. 2). We then compared FA along the optic nerve between the SMS rsEPI and SMS ssEPI datasets.

Figure 3 depicts the profile of FA along the optic nerve in the SMS rsEPI (red) and SMS ssEPI datasets (blue) acquired in Experiment 1. In both hemispheres, the SMS rsEPI dataset exhibited a higher FA than the SMS ssEPI dataset. The differences were more prominent at the middle part of the optic nerve than at the anterior and posterior end. We then performed a statistical comparison between the datasets, by comparing the FA values averaged across all nodes along the optic nerve (Fig. 3, right panel). In both hemispheres, SMS rsEPI data exhibited significantly higher FA than SMS ssEPI data along the optic nerve (left hemisphere; d = 0.73; paired *t*-test, t_{10} = 6.42; 95% confidence interval [CI] = 0.03–0.06, $P < 0.001$; right hemisphere; d = 0.99; paired t-test, t_{10} = 6.50; 95% CI = 0.03–0.06, $P < 0.001$).

Figure 4 depicts the optic nerve results in Experiment 2, in which dMRI data were acquired with the smaller voxel size. Consistent with the results of Experiment 1, SMS rsEPI data showed a higher FA than SMS ssEPI data in the optic nerve (Fig. 4). Statistical comparisons suggest that SMS rsEPI exhibited significantly higher FA than SMS ssEPI data along the optic nerve (left hemisphere; d = 0.88; paired *t*-test, t_{10} = 7.47; 95% CI = 0.04–0.07, $P < 0.001$; right hemisphere; d = 1.05; paired *t*-test, t_{10} = 10.01; 95% CI = 0.04–0.06, $P < 0.001$). Taken together, these results indicate that SMS rsEPI data showed higher FA values along the optic nerve in the two datasets with different voxel sizes even after the susceptibility-induced distortion was corrected.

In the supplementary analysis, SMS rsEPI did not significantly differ in terms of FA between Experiment 1 and 2 (left hemisphere: d = 0.14; paired t-test, t_{10} = 0.94; 95% CI = −0.01 - 0.03, $P = 0.37$; right hemisphere: d = 0.03; paired t-test, t_{10} = 0.15; 95% CI = −0.02 - 0.02, $P = 0.88$). In the left hemisphere, SMS ssEPI data acquired with a larger voxel size (Experiment 1) exhibited significantly higher FA values than those in Experiment 2 (d = 0.30; paired t-test, t_{10} = 3.01; 95% CI = 0.00–0.03, $P = 0.01$). However, the difference was not significant in the right hemisphere (d = 0.18; paired t-test, t_{10} = 0.80; 95% CI = −0.01 - 0.03, $P = 0.44$).

FA was computed from the AD and RD. We also examined these variables to better understand the source of the increased FA values along the optic nerve in the SMS rsEPI dataset. In both Experiments 1 and 2, the SMS rsEPI dataset showed larger AD and RD values than the SMS ssEPI datasets (Supplementary Fig. 4). The effect size of the difference was much larger in AD (Experiment 1, d = 2.22 and 2.33; Experiment 2, d = 2.77 and 1.89 for left and right hemisphere, respectively) than that in RD (Experiment 1, d = 1.44 and 1.51; Experiment 2, d = 1.82 and 1.23 for left and right hemisphere, respectively). Therefore, while SMS rsEPI data showed increased diffusivity in both the axial and radial directions, the increased sensitivity for AD explains the increased FA in the SMS rsEPI dataset.

In the main analyses, we analyzed tissue properties along the optic nerve in SMS rsEPI and SMS ssEPI by using tractography performed on the SMS rsEPI dataset to match the definition of the tract and voxels belonging to the optic nerve between the datasets. These procedures can potentially bias measurements in the SMS ssEPI dataset if there are any remaining image distortions even after preprocessing and the optic nerve voxels identified in SMS rsEPI data do not precisely match those in the SMS ssEPI dataset. To address this concern, we compared the FA values along the optic nerve when the tract was identified by tractography performed on each dMRI dataset (SMS rsEPI and SMS ssEPI). Even in this case, SMS rsEPI data showed higher FA values than SMS ssEPI data (Supplementary Fig. 5; Experiment 1: d = 0.57 and 0.68; Experiment 2: d = 0.75 and 0.86 for left and right hemisphere, respectively).

3.2.2. Optic tract

We then analyzed the optic tract (Fig. 5A), which is a white matter tract from the optic chiasm to the LGN. While the optic tract also belongs to the early visual white matter pathways, it is in a more posterior and

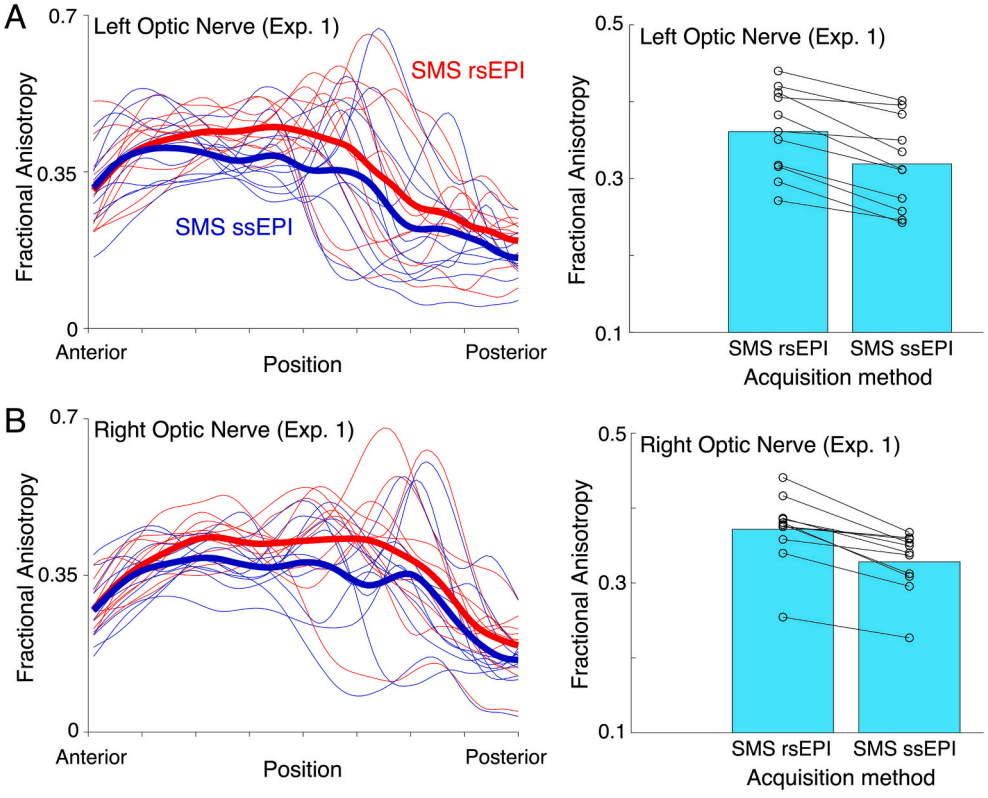

Fig. 3. Comparisons of FA along the optic nerve between the SMS rsEPI and SMS ssEPI datasets in Experiment 1. A. Results for the left optic nerve. *Left panel*: The FA profile along the left optic nerve. The horizontal axis depicts the position along the tract (left, anterior; right, posterior), while the vertical axis depicts the FA. Thick curves depict FA averaged across all participants in each dataset (red, SMS rsEPI; blue, SMS ssEPI). Thin curves indicate the FA values of individual participants in each dataset. *Right panel*: Comparison of FA values averaged across nodes in each participant. Bars indicate FA values averaged across participants. Dots and lines depict data of individual participants. B. Results for the right optic nerve. Conventions are identical to those used in panel A. (For interpretation of the references to colour in this figure legend, the reader is referred to the web version of this article.)

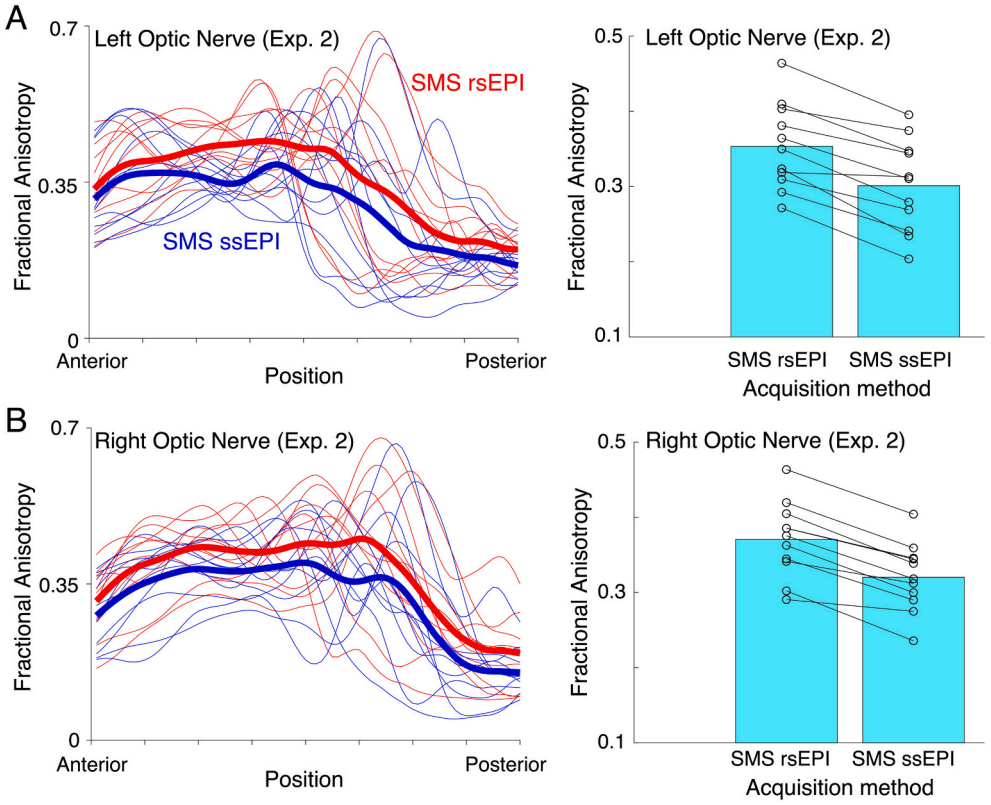

Fig. 4. Comparisons of FA along the optic nerve between the SMS rsEPI and SMS ssEPI datasets in Experiment 2. A. Left optic nerve. B. Right optic nerve. Conventions are identical to those used in Fig. 3.

superior position and may be relatively less affected by susceptibility-induced artifacts than the optic nerve. We evaluated the FA along the optic tract in the SMS rsEPI and SMS ssEPI datasets.

In Experiment 1, similar to the optic nerve, we found that the SMS rsEPI data showed significantly higher FA than the SMS ssEPI data in either hemisphere (Fig. 5B; left hemisphere, d = 1.07; paired *t*-test, t_{10} = 3.87; 95% CI = 0.01–0.05, P = 0.003; right hemisphere, d = 1.01; paired t-test, t_{10} = 4.66; 95% CI = 0.02–0.05, $P < 0.001$). The SMS rsEPI data also showed significantly higher FA than the SMS ssEPI data in Experiment 2 (Fig. 5C; left hemisphere, d = 1.39; paired t-test, t_{10} = 5.09; 95% CI = 0.03–0.07, $P < 0.001$; right hemisphere, d = 1.58, paired t-test, t_{10} = 7.70, 95% CI = 0.03–0.06, $P < 0.001$). These results suggest that an increased FA was observed in the optic tract in the SMS rsEPI dataset compared with SMS ssEPI dataset.

3.2.3. Optic radiation

We also analyzed the optic radiation (Fig. 6A), which is a white matter tract connecting the LGN and V1. The optic radiation is in an even more posterior and superior position than the optic tract. Therefore, this tract may be affected by susceptibility-induced artifacts to a lesser extent.

In Experiment 1, we did not find significant differences in FA between SMS rsEPI and SMS ssEPI data in either hemisphere (Fig. 6B; left hemisphere, d = 0.07, paired *t*-test, t_{10} = 1.07, 95% CI = 0.00–0.01, P = 0.31; right hemisphere, d = 0.10; paired t-test, t_{10} = 1.43; 95% CI = 0.00–0.01, P = 0.18). In Experiment 2, we also did not find a statistically significant difference in FA between the SMS rsEPI and SMS ssEPI datasets (Fig. 6C; left hemisphere, d = 0.01, paired t-test, t_{10} = 0.14, 95% CI = −0.01 - 0.01, P = 0.89; right hemisphere, d = 0.01; paired t-test, t_{10} = 0.09; 95% CI = −0.01 - 0.01, P = 0.93). These results suggest that the FA differences observed in the optic nerve and optic tract were not generalizable to optic radiation.

3.3. Comparisons of diffusivity measurements in other white matter tracts

We also analyzed six major white matter tracts (Fig. 7A; left and right CST, forceps major, forceps minor, and left and right ILF) and compared FA between the SMS rsEPI and SMS ssEPI datasets. In Experiment 1, SMS rsEPI data showed higher FA values than SMS ssEPI data along the right ILF (d = 0.49; t_{10} = 10.60; $P < 0.001$). However, we did not find significant differences between the datasets in the other five tracts (d = 0.01, 0.24, 0.06, −0.01, and 0.08; t_{10} = 0.31, 3.10, 2.10, −0.06, and 1.36; P = 0.76, 0.01, 0.06, 0.95, and 0.20 for the left and right CST, forceps major, forceps minor, and left ILF, respectively). In Experiment 2, SMS rsEPI data showed significantly higher FA values than SMS ssEPI data in the right CST and ILF (d = 0.37 and 0.33; t_{10} = 4.69 and 9.82, respectively; $P < 0.001$ in both tracts). In contrast, we did not find any significant differences between the datasets in the other four tracts (d = −0.04, −0.09, 0.11, and 0.02; t_{10} = −0.33, −1.26, 0.59, and 0.17; P = 0.75, 0.24, 0.57, and 0.87 for the left CST, forceps major, forceps minor, and left ILF, respectively).

4. Discussion

In this study, we evaluated the advantages of SMS rsEPI over SMS ssEPI in dMRI measurements of white matter tracts. We particularly focused on the optic nerve because optic nerve assessments are important to evaluate the consequences of visual disorders. However, they are often affected by susceptibility-induced artifacts in conventional SMS ssEPI acquisition [31]. We visually confirmed that the SMS rsEPI data showed smaller amounts of susceptibility-induced distortions near the optic nerve than SMS ssEPI data, indicating the advantage of SMS rsEPI in measuring this tract. Even after distortion correction, the SMS rsEPI dataset showed higher FA values along the optic nerve than the SMS ssEPI dataset. The increase in FA values along the optic nerve was consistently observed in two datasets acquired with different voxel sizes

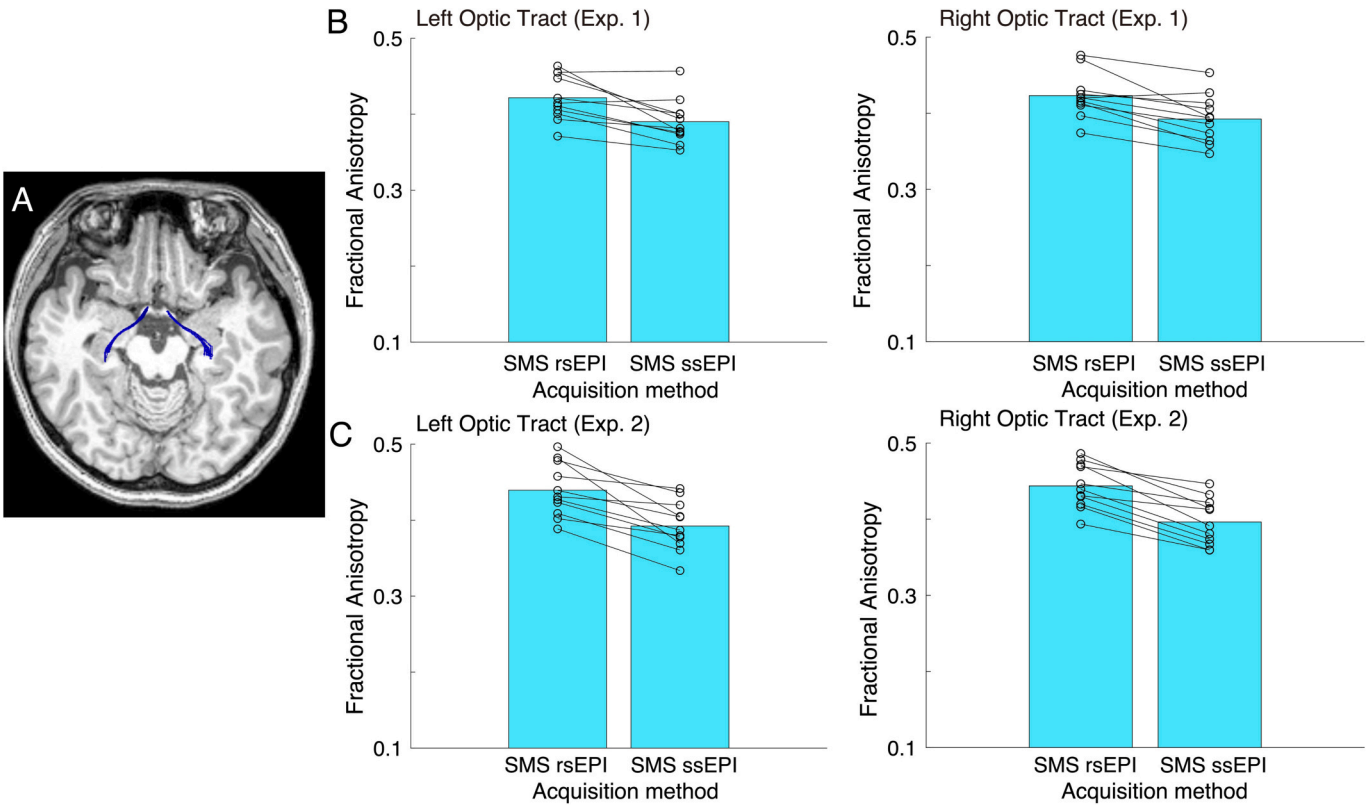

Fig. 5. Comparisons of FA along the optic tract between the SMS rsEPI and SMS ssEPI datasets. A. The optic tract (blue) identified by tractography on SMS rsEPI data acquired from a representative participant (participant P1). The optic tract was overlaid on an axial slice of a T1-weighted image of a region located inferior to the tract. B-C. FA along the optic tract in the SMS rsEPI and SMS ssEPI dataset (B. Experiment 1; C. Experiment 2). (For interpretation of the references to colour in this figure legend, the reader is referred to the web version of this article.)

and also observed in the optic tract. In contrast, the increase of FA values was insignificant in some other major white matter tracts, such as the optic radiation, suggesting that the effect observed in early visual pathways is not generalizable to the entire white matter. In summary, our results demonstrate that SMS rsEPI is a promising approach for measuring the tissue properties of white matter tracts affected by susceptibility-induced artifacts, such as the optic nerve.

4.1. SMS rsEPI shows smaller distortion and higher FA in dMRI measurements of the optic nerve

This study aimed to investigate the advantages of the SMS rsEPI method in comparison with SMS ssEPI for dMRI measurements on the human optic nerve. Our results suggested that SMS rsEPI data showed smaller amounts of image distortions (Fig. 2) and higher FA values (Fig. 3) along the optic nerve, supporting the idea that SMS rsEPI will be an advantageous method for dMRI measurements on this pathway. One interpretive limitation of this result is that a higher FA does not always indicate an improvement in the dMRI measurements. Moreover, FA depends on many different factors (partial voluming, crossing fibers, and microstructural properties such as myelination), and the relationship between signal-to-noise ratio and FA can be complex, as demonstrated by a numerical simulation study in which the measurements with lower signal-to-noise ratio induced overestimation or underestimation of FA [81]. Due to a lack of ground truth in the *in vivo* dMRI measurements performed on human brains, the interpretation of increased FA along the optic nerve remains speculative. However, since the optic nerve does not cross other tracts and most optic nerve fibers are myelinated [82], the optic nerve should show a higher FA value if the measurement does not suffer from lower signal quality and artifacts. Therefore, a lower FA value along the optic nerve observed in the SMS ssEPI dataset may reflect the limited sensitivity of dMRI measurements in identifying diffusion anisotropy that must exist in the optic nerve. However, the same interpretation for FA results will not be applicable to other tracts such as the ILF, which include regions that cross other fiber tracts [83].

Several possible reasons can be used to explain the source of FA differences in the optic nerve between the SMS rsEPI and SMS ssEPI datasets. The first possible reason is the influence of the longer echo train in SMS ssEPI than that in SMS rsEPI. It seems likely that T_2* decay during the longer echo train affected the point spread function and consequently caused blurring and partial volume effects in the SMS ssEPI dataset. The second possible reason is that an increased level of distortion in the SMS ssEPI images results in blurring after distortion correction during preprocessing, and this blurring effect can be greater than when the same procedure is applied to SMS rsEPI. This blurring effect may result in reduced FA in the SMS ssEPI dataset. Lastly, it is also possible that differences in general image quality and noise distribution between the datasets may result in FA differences. It is known that noise of MRI data with a lower signal-to-noise ratio follows non-Gaussian distribution [84]. Such noise distribution may affect the estimation of diffusivity measurements [85]. If this effect is more substantial in SMS ssEPI images rather than SMS rsEPI images, such difference can also cause FA differences, as observed in this study. Of note, images acquired via SMS rsEPI and SMS ssEPI were reconstructed through different processes, as SMS rsEPI data from multiple shots are combined in k-space before conversion to modulus images. This difference may impact the noise distributions.

The impact of some of the aforementioned factors might significantly depend on the acquisition parameters selected, such as the b-value and voxel size, since these can affect the achievable echo spacing in the EPI echo train. In this study, we performed two experiments with different voxel sizes (2 mm and 1.8 mm isotropic) and found that dependencies on

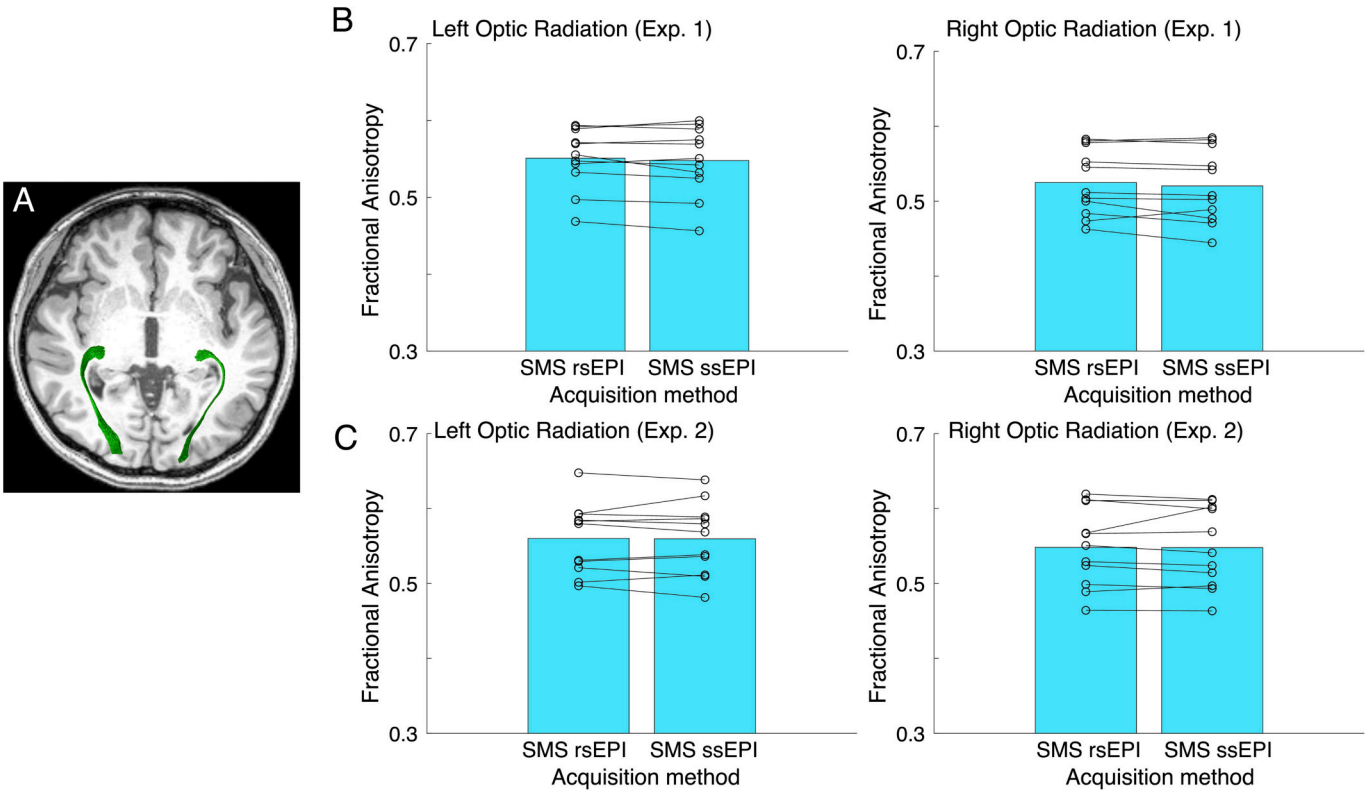

Fig. 6. Comparisons of FA along the optic radiation between SMS rsEPI and SMS ssEPI datasets. A. The optic radiation (green) identified by tractography on SMS rsEPI data acquired from a representative participant (participant P1). The optic radiation was overlaid on an axial slice of a T1-weighted image of a region located inferior to the tract. B-C. FA along the optic radiation in the SMS rsEPI and SMS ssEPI datasets (B. Experiment 1; C. Experiment 2). (For interpretation of the references to colour in this figure legend, the reader is referred to the web version of this article.)

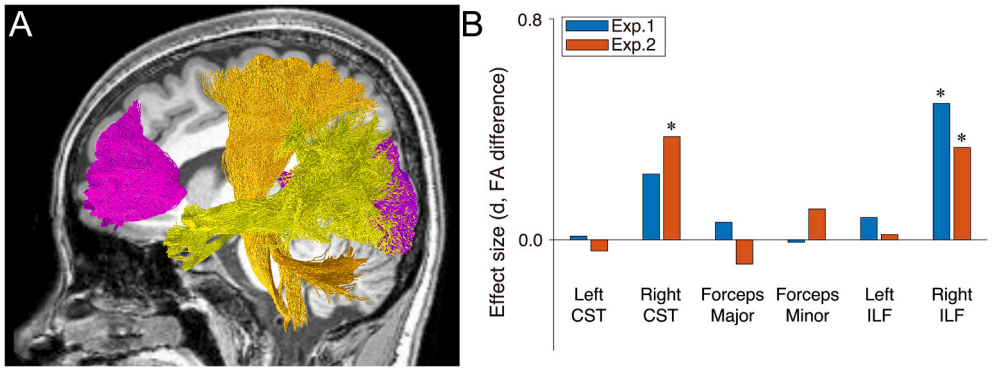

Fig. 7. Comparisons of FA along other major tracts between SMS rsEPI and SMS ssEPI datasets. A. The left corticospinal tract (CST, orange), forceps major (purple), forceps minor (magenta), and left inferior longitudinal fasciculus (ILF, yellow) identified by tractography on SMS rsEPI data acquired from a representative participant (participant P1) overlaid on a sagittal slice of a T1-weighted image, which is located medial to the CST and ILF. B. Effect size (d, vertical axis) on the FA difference between SMS rsEPI and SMS ssEPI datasets in white matter tracts (blue, Exp. 1; red, Exp. 2). A positive value indicates that FA was higher in the SMS rsEPI dataset than in the SMS ssEPI dataset. Asterisk indicates statistical significance ($P < 0.004$). (For interpretation of the references to colour in this figure legend, the reader is referred to the web version of this article.)

the voxel size may be small or absent in the optic nerve (Figs. 3 and 4). However, we may observe dependencies on the voxel size if we test different combinations of voxel size and other parameters, such as the b-value. Since it was difficult to test all combinations of the acquisition parameters in a single study, dependencies on the acquisition parameters should be further assessed in future investigations.

4.2. Dependency on white matter tracts

Our results also suggest that the potential advantage of SMS rsEPI depends on the white matter tracts. For example, the optic radiation did not show statistically significant differences between the SMS rsEPI and SMS ssEPI datasets in either experiment (Fig. 6). This is most likely because the optic radiation is not located near the paranasal sinus, and dMRI measurements of this tract are less affected by susceptibility-induced distortion. In fact, previous studies have demonstrated that it is quite possible to identify the optic radiation and its tissue changes caused by retinal disorders by using the ssEPI approach [9,11]. However, we did not exclude the possibility that the advantage of SMS rsEPI is smaller in the optic radiation, since FA measurements do not strongly reflect the improvement of signal quality because the structural properties of the tract (tract size and crossing fibers) differ from those of the optic nerve [72].

We also found that some association pathways, such as the right ILF, showed higher FA values in the SMS rsEPI dataset (Fig. 7). This result can be explained by the fact that the ILF is located close to the temporal

pole, which is an area often affected by susceptibility-induced artifacts due to its proximity to the petrous apex and mastoid air complexes.

4.3. Limitations and future directions

One notable limitation of this study is that we only tested one hardware (SIEMENS MAGNETOM 3 T Prisma) for comparisons between SMS rsEPI and SMS ssEPI. While this magnet has a high-performance gradient system (maximum gradient amplitude: 80 mT/m, slew rate: 200 mT/m/s), the disadvantages of SMS ssEPI can be reduced if MR systems with ultra-high-performance gradient coils become widely available, because such systems can substantially reduce echo spacing and TE on dMRI measurements using SMS ssEPI [86,87]. In contrast, the advantage of SMS rsEPI may become much larger when using an MR system with a higher static magnetic field (7 T or beyond), in which the limitations imposed by T_2* decay became more challenging [53]. For these reasons, the advantages of SMS rsEPI over SMS ssEPI, as shown in this study, are not fully generalizable to other hardwares with different gradient performance levels and static magnetic field strengths.

SMS acquisition is very effective when a large number of slices are necessary to cover the whole brain. It is particularly useful when researchers aim to evaluate the impact of disease on the optic nerve, together with other white matter tracts, such as the optic tract, optic radiation, and other association pathways. However, if smaller coverage is adequate, rsEPI without SMS acquisition may be more advantageous for measurement of the optic nerve as this may avoid the signal-to-noise ratio reduction associated with SMS. This point needs to be clarified by future studies in which rsEPI with and that without SMS are compared.

While this study focused entirely on healthy young adult participants, future investigations should be performed on clinical populations with various ages to validate the clinical benefits of SMS rsEPI. Since the results of this study demonstrated that SMS rsEPI is advantageous for optic nerve measurements, one possible extension of this study is to use SMS rsEPI for acquiring dMRI data from patients with disorders directly affecting the optic nerve, such as glaucoma [12,25,26,29,75] and optic neuritis [24,32,34,36,50,51]. Accurate measurements of the optic nerve will also facilitate evaluations of amblyopia [27,28], in which the degree of decreased vision can differ between the two eyes, necessitating measurement of the tissue properties of the optic nerve in individual hemispheres. The generalizability of our results to participants from different age groups needs to be evaluated, considering the age dependency of dMRI measurements on white matter tracts [18–20,23]. As the prevalence rate of certain visual disorders, such as glaucoma, is higher in older age groups [88], such evaluation is essential to clarify the benefit of SMS rsEPI for clinical practice. Future studies should aim to determine the extent to which SMS rsEPI has improved sensitivity in identifying tissue changes along the optic nerve occurring as a consequence of these visual disorders.

In our study, SMS rsEPI exhibited a smaller amount of image distortion than SMS ssEPI (Fig. 2), which indicates that it holds promise for future application in diagnostic imaging. For further advancement of the clinical application of dMRI, tissue properties of the optic nerve of one individual have to be quantitatively evaluated in relation to the distribution of properties in a healthy population. A tract-specific approach [8,89,90], as performed in this study, is an important step to enable quantitative, statistical evaluation of a specific tract of interest in individual brains. However, further studies on its reliability and generalizability are required to validate an SMS rsEPI-based tractography approach for clinical investigations [91,92]. An extension of this work should provide further insights into how SMS rsEPI can be best used for clinical evaluation of the human optic nerve.

5. Conclusions

This study demonstrated that dMRI acquisition with SMS rsEPI offered advantages in measurement of the optic nerve in comparison with SMS ssEPI in terms of reduced susceptibility-induced artifacts and increased diffusion anisotropy along the tract. This result will open up avenues to perform health- and disease-related investigations on optic nerve tissue properties with a reasonable acquisition time.

Ethics statement

The study protocol was approved by the local ethics and safety committees at Center for Information and Neural Networks (CiNet), Advanced ICT Research Institute, National Institute of Information and Communications Technology (NICT) and conducted in accordance with the ethical standards stated in the Declaration of Helsinki. Written informed consent was obtained from all study participants.

Funding

This study was supported by the Japan Society for the Promotion of Science (JSPS) KAKENHI (JP17H04684 and JP21H03789 to H.T.). The funders had no role in study design, data collection and analysis, decision to publish, or preparation of the manuscript.

CRediT authorship contribution statement

Hiromasa Takemura: Conceptualization, Data curation, Formal analysis, Funding acquisition, Investigation, Methodology, Validation, Visualization, Writing – original draft, Writing – review & editing. **Wei Liu:** Methodology, Resources, Writing – review & editing. **Hideto Kuribayashi:** Resources, Writing – review & editing. **Toshikazu Miyata:** Formal analysis, Investigation, Methodology, Visualization, Writing – review & editing. **Ikuhiro Kida:** Conceptualization, Project administration, Supervision, Writing – original draft, Writing – review & editing.

Declaration of Competing Interest

WL and HK are employed by Siemens Healthcare. Siemens Healthcare did not have any additional role in the study design, data collection and analysis. Other three authors have declared that no competing interests exist.

Acknowledgments

We thank Dr. Hiroki Oishi, Mr. Yusuke Sakai, and Ms. Hiroko Fujimoto in support of data acquisition.

Appendix A. Supplementary data

Supplementary data to this article can be found online at https://doi.org/10.1016/j.mri.2023.05.001.

References

[1] Wandell BA. Clarifying human white matter. Annu Rev Neurosci 2016;39:103–28.
[2] Rokem A, Takemura H, Bock AS, Scherf KS, Behrmann M, Wandell BA, et al. The visual white matter: The application of diffusion MRI and fiber tractography to vision science. J Vis 2017;17(2):4.
[3] Thomason ME, Thompson PM. Diffusion imaging, white matter, and psychopathology. Annu Rev Clin Psychol 2011;7:63–85.
[4] Assaf Y, Johansen-Berg H, Thiebaut de Schotten M. The role of diffusion MRI in neuroscience. NMR Biomed 2019;32:e3762.
[5] Mori S, Zhang J. Principles of diffusion tensor imaging and its applications to basic neuroscience research. Neuron 2006;51:527–39.
[6] Catani M. Thiebaut de Schotten M. Atlas of human brain connections. Oxford University Press; 2012.
[7] Catani M, Thiebaut de Schotten M. A diffusion tensor imaging tractography atlas for virtual in vivo dissections. Cortex 2008;44:1105–32.
[8] Yeatman JD, Dougherty RF, Myall NJ, Wandell BA, Feldman HM. Tract profiles of white matter properties: automating fiber-tract quantification. PLoS One 2012;7:e49790.

[9] Ogawa S, Takemura H, Horiguchi H, Terao M, Haji T, Pestilli F, et al. White matter consequences of retinal receptor and ganglion cell damage. Invest Ophthalmol Vis Sci 2014;55:6976–86.
[10] Yoshimine S, Ogawa S, Horiguchi H, Terao M, Miyazaki A, Matsumoto K, et al. Age-related macular degeneration affects the optic radiation white matter projecting to locations of retinal damage. Brain Struct Funct 2018;223:3889–900.
[11] Takemura H, Ogawa S, Mezer AA, Horiguchi H, Miyazaki A, Matsumoto K, et al. Diffusivity and quantitative T1 profile of human visual white matter tracts after retinal ganglion cell damage. NeuroImage: Clin 2019;23:101826.
[12] Ogawa S, Takemura H, Horiguchi H, Miyazaki A, Matsumoto K, Masuda Y, et al. Multi-contrast magnetic resonance imaging of visual white matter pathways in patients with glaucoma. Invest Ophthalmol Vis Sci 2022;63:29.
[13] Yeatman JD, Dougherty RF, Ben-Shachar M, Wandell BA. Development of white matter and reading skills. Proc Natl Acad Sci U S A 2012;109:E3045–53.
[14] Wandell BA, Yeatman JD. Biological development of reading circuits. Curr Opin Neurobiol 2013;23:261–8.
[15] Huber E, Donnelly PM, Rokem A, Yeatman JD. Rapid and widespread white matter plasticity during an intensive reading intervention. Nat Commun 2018;9:2260.
[16] Thiebaut de Schotten M, Cohen L, Amemiya E, Braga LW, Dehaene S. Learning to read improves the structure of the arcuate fasciculus. Cereb Cortex 2014;24:989–95.
[17] Craig MC, Catani M, Deeley Q, Latham R, Daly E, Kanaan R, et al. Altered connections on the road to psychopathy. Mol Psychiatry 2009;14(946–53):907.
[18] Lebel C, Treit S, Beaulieu C. A review of diffusion MRI of typical white matter development from early childhood to young adulthood. NMR Biomed 2019;32:e3778.
[19] Lebel C, Gee M, Camicioli R, Wieler M, Martin W, Beaulieu C. Diffusion tensor imaging of white matter tract evolution over the lifespan. Neuroimage 2012;60:340–52.
[20] Yeatman JD, Wandell BA, Mezer AA. Lifespan maturation and degeneration of human brain white matter. Nat Commun 2014;5:4932.
[21] Thiebaut de Schotten M, Dell'Acqua F, Forkel SJ, Simmons A, Vergani F, Murphy DG, et al. A lateralized brain network for visuospatial attention. Nat Neurosci 2011;14:1245–6.
[22] Howells H, Thiebaut de Schotten M, Dell'Acqua F, Beyh A, Zappalà G, Leslie A, et al. Frontoparietal tracts linked to lateralized hand preference and manual specialization. Cereb Cortex 2018;28:2482–94.
[23] Amemiya K, Naito E, Takemura H. Age dependency and lateralization in the three branches of the human superior longitudinal fasciculus. Cortex 2021;139:116–33.
[24] Raz N, Bick AS, Ben-Hur T, Levin N. Focal demyelinative damage and neighboring white matter integrity: an optic neuritis study. Mult Scler 2015;21:562–71.
[25] Gupta N, Yücel YH. What changes can we expect in the brain of glaucoma patients? Surv Ophthalmol 2007;52(Suppl. 2):S122–6.
[26] Miller N, Liu Y, Krivochenitser R, Rokers B. Linking neural and clinical measures of glaucoma with diffusion magnetic resonance imaging (dMRI). PLoS One 2019;14:e0217011.
[27] Allen B, Schmitt MA, Kushner BJ, Rokers B. Retinothalamic white matter abnormalities in amblyopia. Invest Ophthalmol Vis Sci 2018;59:921–9.
[28] Allen B, Spiegel DP, Thompson B, Pestilli F, Rokers B. Altered white matter in early visual pathways of human amblyopes. Vis Res 2015;114:48–55.
[29] Omodaka K, Murata T, Sato S, Takahashi M, Tatewaki Y, Nagasaka T, et al. Correlation of magnetic resonance imaging optic nerve parameters to optical coherence tomography and the visual field in glaucoma. Clin Exp Ophthalmol 2014;42:360–8.
[30] Moon Y, Yang J-J, Lee WJ, Lee JY, Kim YJ, Lim HW. Alzheimer's Disease Neuroimaging Initiative (ADNI). In vivo analysis of normal optic nerve in an elderly population using diffusion magnetic resonance imaging tractography. Front Neurol 2021;12:680488.
[31] Hoch MJ, Bruno MT, Shepherd TM. Advanced MRI of the optic nerve. J Neuroophthalmol 2017;37:187–96.
[32] Kolbe S, Chapman C, Nguyen T, Bajraszewski C, Johnston L, Kean M, et al. Optic nerve diffusion changes and atrophy jointly predict visual dysfunction after optic neuritis. Neuroimage 2009;45:679–86.
[33] Wheeler-Kingshott CAM, Trip SA, Symms MR, Parker GJM, Barker GJ, Miller DH. In vivo diffusion tensor imaging of the human optic nerve: Pilot study in normal controls. Magn Reson Med 2006;56:446–51.
[34] Trip SA, Wheeler-Kingshott C, Jones SJ, Li W-Y, Barker GJ, Thompson AJ, et al. Optic nerve diffusion tensor imaging in optic neuritis. Neuroimage 2006;30:498–505.
[35] Wheeler-Kingshott CAM, Parker GJM, Symms MR, Hickman SJ, Tofts PS, Miller DH, et al. ADC mapping of the human optic nerve: increased resolution, coverage, and reliability with CSF-suppressed ZOOM-EPI. Magn Reson Med 2002;47:24–31.
[36] Hickman SJ, Wheeler-Kingshott CAM, Jones SJ, Miszkiel KA, Barker GJ, Plant GT, et al. Optic nerve diffusion measurement from diffusion-weighted imaging in optic neuritis. AJNR Am J Neuroradiol 2005;26:951–6.
[37] Jeong H-K, Dewey BE, Hirtle JAT, Lavin P, Sriram S, Pawate S, et al. Improved diffusion tensor imaging of the optic nerve using multishot two-dimensional navigated acquisitions. Magn Reson Med 2015;74:953–63.
[38] Butts K, Pauly J, de Crespigny A, Moseley M. Isotropic diffusion-weighted and spiral-navigated interleaved EPI for routine imaging of acute stroke. Magn Reson Med 1997;38:741–9.
[39] Pipe JG, Farthing VG, Forbes KP. Multishot diffusion-weighted FSE using PROPELLER MRI. Magn Reson Med 2002;47:42–52.
[40] Miller KL, Pauly JM. Nonlinear phase correction for navigated diffusion imaging. Magn Reson Med 2003;50:343–53.
[41] Liu C, Bammer R, Kim D-H, Moseley ME. Self-navigated interleaved spiral (SNAILS): application to high-resolution diffusion tensor imaging. Magn Reson Med 2004;52:1388–96.
[42] Pipe JG, Zwart N. Turboprop: improved PROPELLER imaging. Magn Reson Med 2006;55:380–5.
[43] Jeong H-K, Gore JC, Anderson AW. High-resolution human diffusion tensor imaging using 2-D navigated multishot SENSE EPI at 7 T. Magn Reson Med 2013;69:793–802.
[44] Chen N-K, Guidon A, Chang H-C, Song AW. A robust multi-shot scan strategy for high-resolution diffusion weighted MRI enabled by multiplexed sensitivity-encoding (MUSE). Neuroimage 2013;72:41–7.
[45] Bilgic B, Chatnuntawech I, Manhard MK, Tian Q, Liao C, Iyer SS, et al. Highly accelerated multishot echo planar imaging through synergistic machine learning and joint reconstruction. Magn Reson Med 2019;82:1343–58.
[46] Porter DA, Heidemann RM. High resolution diffusion-weighted imaging using readout-segmented echo-planar imaging, parallel imaging and a two-dimensional navigator-based reacquisition. Magn Reson Med 2009;62:468–75.
[47] Zhou F, Li Q, Zhang X, Ma H, Zhang G, Du S, et al. Reproducibility and feasibility of optic nerve diffusion MRI techniques: single-shot echo-planar imaging (EPI), readout-segmented EPI, and reduced field-of-view diffusion-weighted imaging. BMC Med Imaging 2022;22:1–11.
[48] Chen HH, Hu H, Chen W, Cui D, Xu XQ, Wu FY, et al. Thyroid-associated orbitopathy: evaluating microstructural changes of extraocular muscles and optic nerves using readout-segmented echo-planar imaging-based diffusion tensor imaging. Korean J Radiol 2020;21:332–40.
[49] Yeom KW, Holdsworth SJ, Van AT, Iv M, Skare S, Lober RM, et al. Comparison of readout-segmented echo-planar imaging (EPI) and single-shot EPI in clinical application of diffusion-weighted imaging of the pediatric brain. AJR Am J Roentgenol 2013;200:W437–43.
[50] Wan H, Sha Y, Zhang F, Hong R, Tian G, Fan H. Diffusion-weighted imaging using readout-segmented echo-planar imaging, parallel imaging, and two-dimensional navigator-based reacquisition in detecting acute optic neuritis. J Magn Reson Imaging 2016;43:655–60.
[51] Seeger A, Schulze M, Schuettauf F, Ernemann U, Hauser T-K. Advanced diffusion-weighted imaging in patients with optic neuritis deficit - value of reduced field of view DWI and readout-segmented DWI. Neuroradiol J 2018;31:126–32.
[52] Yamada H, Yamamoto A, Okada T, Kanagaki M, Fushimi Y, Porter DA, et al. Diffusion tensor imaging of the optic chiasm in patients with intra- or parasellar tumor using readout-segmented echo-planar. Magn Reson Imaging 2016;34:654–61.
[53] Kida I, Ueguchi T, Matsuoka Y, Zhou K, Stemmer A, Porter D. Comparison of diffusion-weighted imaging in the human brain using readout-segmented EPI and PROPELLER turbo spin echo with single-shot EPI at 7 T MRI. Investig Radiol 2016;51:435–9.
[54] Larkman DJ, Hajnal JV, Herlihy AH, Coutts GA, Young IR, Ehnholm G. Use of multicoil arrays for separation of signal from multiple slices simultaneously excited. J Magn Reson Imaging 2001;13:313–7.
[55] Breuer FA, Blaimer M, Heidemann RM, Mueller MF, Griswold MA, Jakob PM. Controlled aliasing in parallel imaging results in higher acceleration (CAIPIRINHA) for multi-slice imaging. Magn Reson Med 2005;53:684–91.
[56] Setsompop K, Cohen-Adad J, Gagoski BA, Raij T, Yendiki A, Keil B, et al. Improving diffusion MRI using simultaneous multi-slice echo planar imaging. Neuroimage 2012;63:569–80.
[57] Frost R, Jezzard P, Douaud G, Clare S, Porter DA, Miller KL. Scan time reduction for readout-segmented EPI using simultaneous multislice acceleration: Diffusion-weighted imaging at 3 and 7 Tesla. Magn Reson Med 2015;74:136–49.
[58] Setsompop K, Gagoski BA, Polimeni JR, Witzel T, Wedeen VJ, Wald LL. Blipped-controlled aliasing in parallel imaging for simultaneous multislice echo planar imaging with reduced g-factor penalty. Magn Reson Med 2012;67:1210–24.
[59] Griswold MA, Jakob PM, Heidemann RM, Nittka M, Jellus V, Wang J, et al. Generalized autocalibrating partially parallel acquisitions (GRAPPA). Magn Reson Med 2002;47:1202–10.
[60] Fischl B. FreeSurfer. Neuroimage 2012;62:774–81.
[61] Zhang Y, Brady M, Smith S. Segmentation of brain MR images through a hidden Markov random field model and the expectation-maximization algorithm. IEEE Trans Med Imaging 2001;20:45–57.
[62] Andersson JLR, Skare S, Ashburner J. How to correct susceptibility distortions in spin-echo echo-planar images: application to diffusion tensor imaging. Neuroimage 2003;20:870–88.
[63] Andersson JLR, Sotiropoulos SN. An integrated approach to correction for off-resonance effects and subject movement in diffusion MR imaging. Neuroimage 2016;125:1063–78.
[64] Leemans A, Jones DK. The B-matrix must be rotated when correcting for subject motion in DTI data. Magn Reson Med 2009;61:1336–49.
[65] Chang L-C, Jones DK, Pierpaoli C. RESTORE: robust estimation of tensors by outlier rejection. Magn Reson Med 2005;53:1088–95.
[66] Basser PJ, Pierpaoli C. Microstructural and physiological features of tissues elucidated by quantitative-diffusion-tensor MRI. J Magn Reson B 1996;111:209–19.
[67] Tournier J-D, Smith R, Raffelt D, Tabbara R, Dhollander T, Pietsch M, et al. MRtrix3: A fast, flexible and open software framework for medical image processing and visualisation. Neuroimage 2019;202:116137.
[68] Fischl B, Rajendran N, Busa E, Augustinack J, Hinds O, Yeo BTT, et al. Cortical folding patterns and predicting cytoarchitecture. Cereb Cortex 2007;18:1973–80.

[69] Tournier J-D, Calamante F, Connelly A. Improved probabilistic streamlines tractography by 2nd order integration over fibre orientation distributions. Proc Int Soc Magn Reson Med 2010;1670.
[70] Sherbondy AJ, Dougherty RF, Ben-Shachar M, Napel S, Wandell BA. ConTrack: finding the most likely pathways between brain regions using diffusion tractography. J Vis 2008;8(9):15.1-16.
[71] Sherbondy AJ, Dougherty RF, Napel S, Wandell BA. Identifying the human optic radiation using diffusion imaging and fiber tractography. J Vis 2008;8(10):12.1-11.
[72] Chamberland M, Scherrer B, Prabhu SP, Madsen J, Fortin D, Whittingstall K, et al. Active delineation of Meyer's loop using oriented priors through MAGNEtic tractography (MAGNET). Hum Brain Mapp 2017;38:509–27.
[73] Levin N, Dumoulin SO, Winawer J, Dougherty RF, Wandell BA. Cortical maps and white matter tracts following long period of visual deprivation and retinal image restoration. Neuron 2010;65:21–31.
[74] Malania M, Konrad J, Jägle H, Werner JS, Greenlee MW. Compromised integrity of central visual pathways in patients with macular degeneration. Invest Ophthalmol Vis Sci 2017;58:2939–47.
[75] Kaushik M, Graham SL, Wang C, Klistorner A. A topographical relationship between visual field defects and optic radiation changes in glaucoma. Invest Ophthalmol Vis Sci 2014;55:5770–5.
[76] Duan Y, Norcia AM, Yeatman JD, Mezer A. The structural properties of major white matter tracts in strabismic amblyopia. Invest Ophthalmol Vis Sci 2015;56:5152–60.
[77] Takemura H, Pestilli F, Weiner KS, Keliris GA, Landi SM, Sliwa J, et al. Occipital white matter tracts in human and macaque. Cereb Cortex 2017;27:3346–59.
[78] You Y, Joseph C, Wang C, Gupta V, Liu S, Yiannikas C, et al. Demyelination precedes axonal loss in the transneuronal spread of human neurodegenerative disease. Brain 2019;142:426–42.
[79] Takemura H, Yuasa K, Amano K. Predicting neural response latency of the human early visual cortex from MRI-based tissue measurements of the optic radiation. eNeuro 2020;7. ENEURO.0545–19.2020.
[80] Smith RE, Tournier JD, Calamante F, Connelly A. Anatomically-constrained tractography: improved diffusion MRI streamlines tractography through effective use of anatomical information. Neuroimage 2012;62:1924–38.
[81] Jones DK, Basser PJ. "Squashing peanuts and smashing pumpkins": how noise distorts diffusion-weighted MR data. Magn Reson Med 2004;52:979–93.
[82] Magoon EH, Robb RM. Development of myelin in human optic nerve and tract. A light and electron microscopic study. Arch Ophthalmol 1981;99:655–9.
[83] Takemura H, Palomero-Gallagher N, Axer M, Gräßel D, Jorgensen MJ, Woods R, et al. Anatomy of nerve fiber bundles at micrometer-resolution in the vervet monkey visual system. Elife 2020;9:e55444.
[84] Gudbjartsson H, Patz S. The Rician distribution of noisy MRI data. Magn Reson Med 1995;34:910–4.
[85] Dietrich O, Heiland S, Sartor K. Noise correction for the exact determination of apparent diffusion coefficients at low SNR. Magn Reson Med 2001;45:448–53.
[86] Huang SY, Witzel T, Keil B, Scholz A, Davids M, Dietz P, et al. Connectome 2.0: Developing the next-generation ultra-high gradient strength human MRI scanner for bridging studies of the micro-, meso- and macro-connectome. Neuroimage 2021;243:118530.
[87] Tan ET, Lee S-K, Weavers PT, Graziani D, Piel JE, Shu Y, et al. High slew-rate head-only gradient for improving distortion in echo planar imaging: preliminary experience. J Magn Reson Imaging 2016;44:653–64.
[88] Iwase A, Suzuki Y, Araie M, Yamamoto T, Abe H, Shirato S, et al. The prevalence of primary open-angle glaucoma in Japanese: the Tajimi Study. Ophthalmology 2004;111:1641–8.
[89] Jones DK, Travis AR, Eden G, Pierpaoli C, Basser PJ. PASTA: pointwise assessment of streamline tractography attributes. Magn Reson Med 2005;53:1462–7.
[90] Colby JB, Soderberg L, Lebel C, Dinov ID, Thompson PM, Sowell ER. Along-tract statistics allow for enhanced tractography analysis. Neuroimage 2012;59:3227–42.
[91] Kruper J, Yeatman JD, Richie-Halford A, Bloom D, Grotheer M, Caffarra S, et al. Evaluating the reliability of human brain white matter tractometry. Aperture Neuro 2021;1. https://doi.org/10.52294/e6198273-b8e3-4b63-babb-6e6b0da10669.
[92] Lerma-Usabiaga G, Mukherjee P, Ren Z, Perry ML, Wandell BA. Replication and generalization in applied neuroimaging. Neuroimage 2019;202:116048.
[93] Echevarria-Cooper SL, Zhou G, Zelano C, Pestilli F, Parrish TB, Kahnt T. Mapping the microstructure and striae of the human olfactory tract with diffusion MRI. J Neurosci 2022;42:58–68.